ACS NANO

www.acsnano.org

ARTICLE

Dual-MOF-Layered Films via Solution Shearing Approach: A Versatile Platform for Tunable Chemiresistive Sensors

Chungseong Park,[§] Junhee Woo,[§] Mingyu Jeon,[§] Jong Won Baek, Euichul Shin, Jihan Kim,* Steve Park,* and Il-Doo Kim*

Cite This: https://doi.org/10.1021/acsnano.4c18848

Read Online

ACCESS | Metrics & More | Article Recommendations | Supporting Information

ABSTRACT: Metal−organic frameworks (MOFs) are ideal for gas sensing due to their high porosity and chemical diversity. However, their low electrical conductivity has traditionally limited their application in chemiresistive-type sensors. The recent development of electrically conductive MOFs (cMOFs) has addressed this limitation. However, directly designing cMOFs with specific sensing properties remains challenging due to the limited understanding of their structure−property relationships. At this stage, the synergistic integration of cMOFs with conventional insulating MOFs has emerged as a viable solution, enabling diverse gas interactions and the rational design of sensing properties. Despite this potential, exploration of the diverse roles of MOFs in such composites remains underutilized. Herein, we develop a series of MOF-on-cMOF sensors and demonstrate their tunable sensing properties. A two-step solution-shearing-based film fabrication method enables facile integration of cMOFs with a wide range of conventional MOFs in layered structures. On cMOF thin film as a primary sensing layer, secondary MOF layers with different pore structures and adsorption properties were strategically selected and deposited. These layered film sensors exhibited tunable sensing properties, including enhanced sensitivity, selectivity, response speed, and recovery for analytes such as NH_3, H_2S, and NO_2. These improvements cannot be achieved solely through the conventional role of MOFs as sieving layers. Furthermore, computational analyses elucidated the structure−property relationships underlying these improvements, offering key insights into the rational design of MOF-based gas sensors.

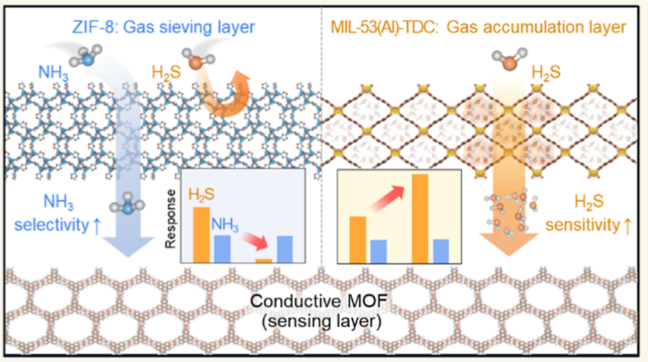

KEYWORDS: *metal−organic frameworks, conductive, layered structures, thin film, gas sensors*

INTRODUCTION

Metal−organic frameworks (MOFs) are viewed as promising gas-sensing materials due to their large surface area and high porosity, which facilitate efficient gas diffusion and adsorption.[1,2] Additionally, MOFs offer extensive chemical diversity due to virtually infinite combinations of linkers and nodes, allowing them to interact with a wide range of analytes. These properties make MOFs versatile and promising for various sensing platforms, including optical,[3] capacitive,[4] and gravimetric sensors.[5] However, their low electrical conductivity has traditionally limited their use in chemiresistive sensing applications.[6] Recently, there have been growing efforts to develop electrically conductive MOFs (cMOFs), which are typically designed with π-conjugated linkers and metal centers to create p-d extended conjugation and p−p orbital overlap, thereby achieving high electrical conductivity.[7] With their high electrical conductivity combined with the inherent advantages of MOFs, cMOFs have emerged as promising materials for chemiresistive sensors, setting them apart from conventional sensing materials.[8,9] While the applicability of cMOF sensors has been demonstrated for various analytes,[10−14] their sensitivity and selectivity have yet to reach sufficient levels. However, directly modifying the structure of cMOFs for desired sensing properties remains challenging due to the incomplete understanding of their structure−property relation-

Received: December 27, 2024
Revised: March 4, 2025
Accepted: March 6, 2025

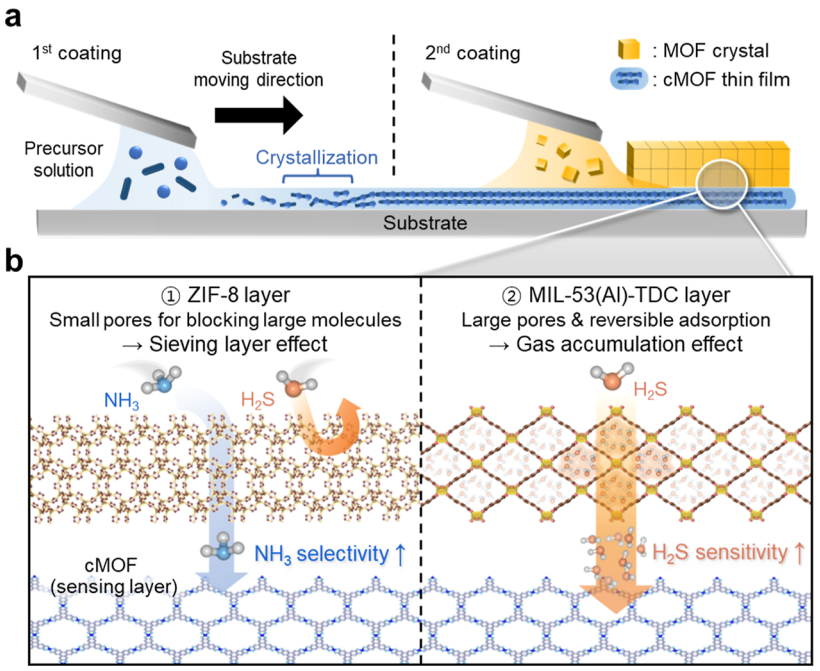

Figure 1. Schematic illustrations of (a) the fabrication process for a layered MOF-on-cMOF film using the solution shearing method and (b) the functional roles of different MOF layers in the gas sensors.

ship. Additionally, maintaining optimal conductivity during the modification process is particularly challenging, even though it is one of the key advantages of cMOFs.[8]

A general strategy to address this issue is to design cMOF-based composites by incorporating other materials with relatively well-understood effects on the sensor properties. Previously, foreign components like metal nanoparticles,[15−17] metal oxides,[18] and conducting polymers[19] have been integrated into cMOF sensors to enhance sensing performance, though this often involved compromise in porosity. An alternative approach is to combine multiple MOFs, which inherently offer high porosities and diverse gas interactions. When integrating cMOFs with other MOFs, two primary approaches are possible. The first involves directly connecting one MOF to another via coordination bonds.[20,21] This method enables strong interactions between the two MOFs but requires complex chemistry and imposes limitations on possible MOF combinations. The second approach entails integrating the two MOFs as separate layers with a van der Waals gap.[22] This configuration supports a broader range of MOF combinations with complementary interactions with gases. Consequently, this strategy holds the potential to improve the sensing performance in diverse ways and across a wide range of target analytes. Despite these advantages, the utilization of MOF layers has been limited to acting as a gas sieving layer for tuning the selectivity. The exploration of this approach beyond conventional applications remains neglected in this field.

In this work, we fabricated a series of MOF-on-cMOF thin film devices using a microfluidic solution shearing process and demonstrated their distinct roles in enhancing the gas-sensing properties. The microfluidic solution shearing method, previously developed by our groups,[23,24] was employed to fabricate highly uniform cMOF thin films with controlled thickness. It served as the primary sensing layer for generating reliable chemiresistive sensing signals. This process was then extended to coat a secondary MOF layer on the cMOF film. During this process, the separately coated MOF layers can preserve the inherent conductive pathways of the cMOF film. Simultaneously, this approach enabled the incorporation of a wide variety of MOFs with different pore structures and gas adsorption properties, allowing for the selection of suitable options for specific target gases. The resulting MOF-on-cMOF devices exhibited diverse effects on the gas sensing performance, including enhanced sensitivity, selectivity, response speed, and recovery for different target analytes, surpassing the conventional role of MOFs as simple gas sieving layers. Furthermore, computational analyses, such as density functional theory (DFT) and molecular dynamics (MD) simulations, were conducted to gain deeper insights into the key properties of MOFs that influence the sensing performance differently.

RESULTS AND DISCUSSION

Preparation of MOF-on-cMOF Thin Films via Solution Shearing. Figure 1a is a schematic illustration of the two-step fabrication process for the MOF-on-cMOF thin film. In the fabrication process, thin films of cMOF and MOF crystals (ZIF-8, MIL-53(Al)-TDC, MIL-53(Fe), and MFM-300(Al)) were sequentially coated by two distinct steps. For the first coating, Cu_3(hexahydroxytriphenylene)$_2$ [Cu_3(HHTP)$_2$], a typical 2D cMOF,[25] was directly synthesized as a thin film on a substrate using a microfluidic blade, which also serves as a solution shearing blade (Figure S1).[26,27] The microfluidic blade is designed with a herringbone pattern for rapid homogeneous mixing of precursor solutions and nucleation (Figures S1c and S2). It ensures the fabrication of highly uniform thin films without aggregation, as demonstrated in our previous research.[23,24] Combined with the subsequent solution shearing process, the thickness of the cMOF film can be regulated to the tens of nanometers scale, which enables efficient mass transport across the entire film. In the second step, a suspension of presynthesized MOF crystals was solidified as the second layer onto the cMOF thin film using

https://doi.org/10.1021/acsnano.4c18848
ACS Nano XXXX, XXX, XXX−XXX

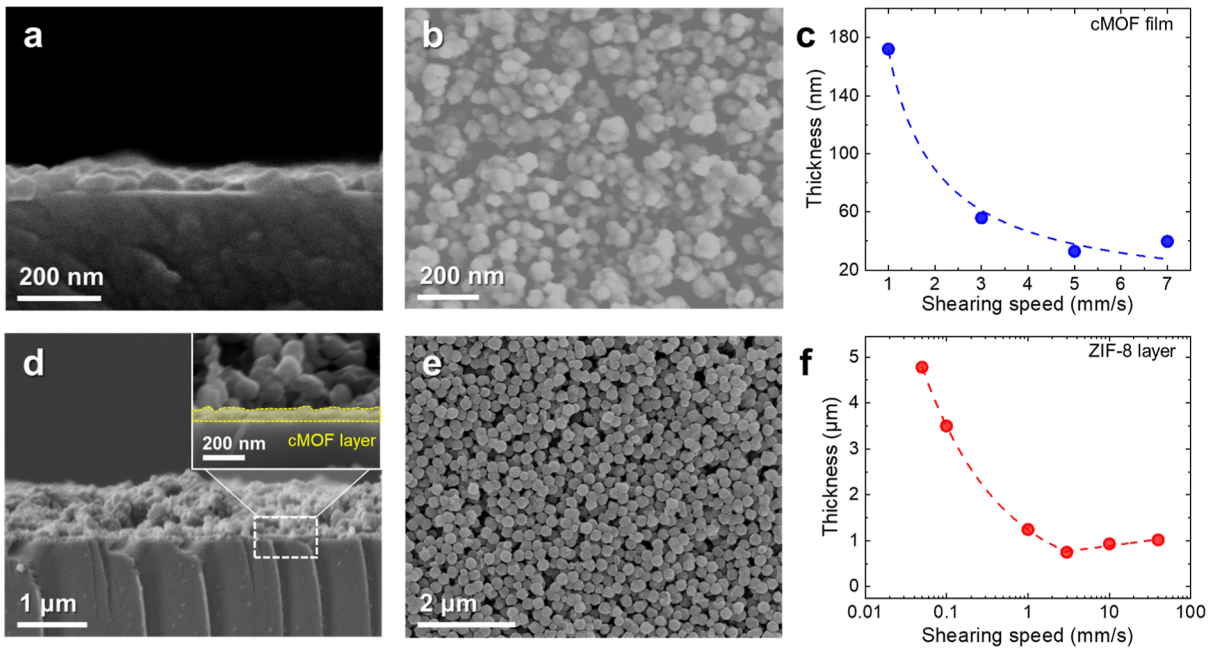

Figure 2. Characterization of MOF-on-cMOF thin films. (a) Cross-sectional SEM image of the cMOF thin film and (b) its top-view SEM image. (c) Thickness variation of the cMOF thin film as a function of the shearing speed, with a fitting curve (thickness ∝ speed$^{-0.98}$ in evaporation regime). (d) Cross-sectional SEM images of the ZIF-8 layer on the cMOF thin film and (e) its top-view SEM image. (f) Thickness variation of the ZIF-8 layer as a function of shearing speed. The fitting curve shows an exponential decrease in thickness for speeds below 3 mm/s (evaporation regime) and a logarithmic increase for speeds above 3 mm/s (Landau−Levich regime).

the solution shearing process. Although directly growing the second MOFs on the cMOF was not possible due to the incompatibility of the synthetic conditions and the limited stability of the cMOF film, this approach enables nearly all types of MOFs to be integrated with the cMOF in a layered structure. Consequently, this fabrication method facilitates the utilization and investigation of various MOF interactions within the hybrid system. Additionally, the thickness of the second MOF layer can also be precisely controlled through solution shearing. The thickness of the MOF overlayer is a critical parameter that governs the inflow flux and penetration depth of the target gas, directly affecting the sensing performance. This two-step process is capable of large-scale production, simultaneously and uniformly yielding about 300 gas sensor devices per batch over an area of 50 × 50 mm (Figure S3). Furthermore, this approach has the potential to be scaled up by increasing the size of the shearing blades and integrating it into roll-to-roll manufacturing processes.[28] Such scalability could greatly enhance large-scale production and quality control, addressing key obstacles to the commercialization of MOF-based sensors.

The sensing properties of cMOF were modulated differently depending on the type of MOF overlayers and their gas interactions. We hypothesized that the sensing properties of MOFs can be tuned in terms of both selectivity and sensitivity through two main mechanisms depending on the pore size and reversibility of gas adsorption: (1) the sieving layer effect and (2) the gas accumulation effect (Figure 1b). Layering MOFs with small pores, comparable to the kinetic diameter of the target gas, results in a well-known gas sieving layer effect and selectivity tuning. For instance, a ZIF-8 overlayer with a pore size of 3.4 Å can selectively allow small NH_3 molecules (kinetic diameter = 2.6 Å) while blocking larger H_2S molecules (3.6 Å).[29] On the other hand, layering MOFs with larger pores and moderate binding energy for the target gas, such as MIL-53(Al)-TDC and MFM-300(Al),[30,31] can induce a gas accumulation effect. These MOFs act as extended gas adsorption sites by allowing the reversible adsorption and desorption of gases, thereby increasing the effective gas concentration near the cMOF sensing layer and improving sensitivity.

Characterization of MOF-on-cMOF Thin Films. Figure 2a,b shows scanning electron microscopy (SEM) images of cMOF thin films fabricated using a microfluidic solution shearing process. Simultaneous synthesis and growth of cMOF during the process enable the formation of cMOF crystallites with an average lateral size of 52.2 nm in the thin film (Figure S4). X-ray diffraction (XRD) patterns of the crystallites obtained from the thin film clearly show the crystal structures of $Cu_3(HHTP)_2$ (Figure S5). As mentioned above, the thickness of the layer is a key factor in sensors, as it directly influences the diffusion and interactions with gas analytes. Therefore, precise control over the layer thickness is crucial for studying and optimizing the sensing properties of MOF-on-cMOF systems. The thickness was finely controlled by the shearing speed of the blade (thickness ∝ speed$^{-0.98}$) down to approximately 30 nm scale, which is consistent with the previous studies (Figure 2c).[23,24]

On the cMOF film, crystallites of various MOFs can be deposited as a second layer through the solution shearing process. Figure 2d,e shows SEM images of the ZIF-8 layer on the cMOF thin film. ZIF-8 crystallites were uniformly deposited on the cMOF thin film with a thickness of 750 nm at a shearing speed of 3 mm/s. Energy-dispersive X-ray spectroscopy (EDS) analysis of the MOF-on-cMOF film further confirmed the formation of two distinct layers (Figure S6). XRD analysis of the second MOF layer reveals that the crystal structure of the MOFs is retained during the solution

https://doi.org/10.1021/acsnano.4c18848
ACS Nano XXXX, XXX, XXX−XXX

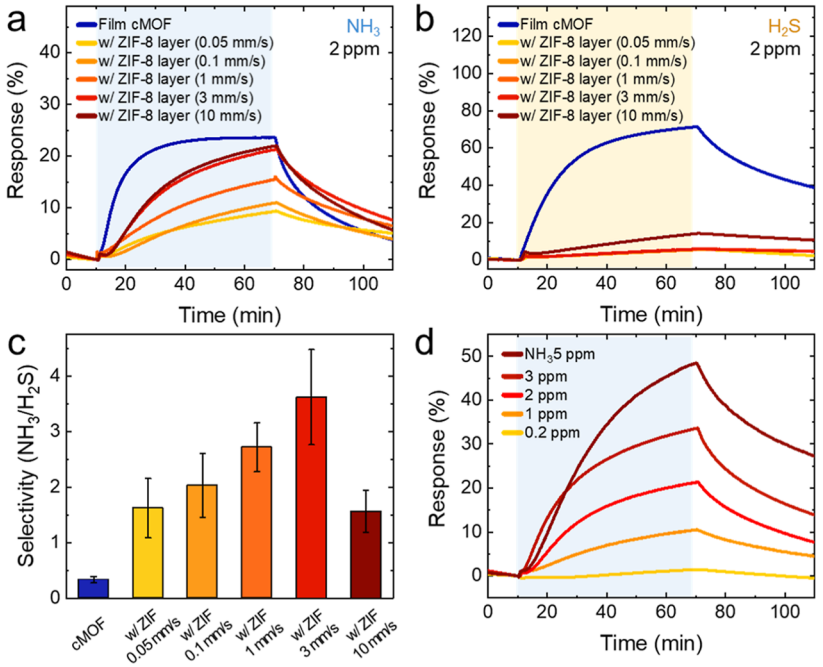

Figure 3. Sensing performances with the ZIF-8 layer. Dynamic sensing traces of the cMOF thin film and ZIF-8 layers fabricated at different shearing speeds toward (a) 2 ppm of NH_3 and (b) H_2S. (c) NH_3/H_2S relative selectivity of a cMOF thin film and ZIF-8 layers fabricated at different shearing speeds. (d) Dynamic sensing traces of the cMOF with a ZIF-8 layer fabricated at a shearing speed of 3 mm/s toward varying concentrations of NH_3.

shearing process (Figure S7). In addition, it was confirmed that other MOFs, including MIL-53(Al)-TDC and MFM-300(Al), can be successfully deposited onto the cMOF layer, demonstrating the versatility of the solution shearing process (Figures S8 and S9). Similar to the coating process for the cMOF film, the thickness of the overlayers can be controlled by adjusting the shearing speed. However, the thickness was controlled on the micron scale, primarily limited by the size of the crystallites (Figure 2f). While higher shearing speeds yield thinner films, increasing the shearing speed beyond a certain point (i.e., evaporation regime) does not further reduce the thickness.[32,33] Instead, as the shearing speed exceeds the rate of solvent evaporation (i.e., Landau−Levich regime), solidification occurs after the formation of a wet film, resulting in lower uniformity (Figure S10 and related discussions in the Supporting Information).[34,35] Nonetheless, submicron thickness can be achieved within the evaporation regime, which corresponds to a few layers of MOF crystallites. Altogether, by utilizing the two-step shearing-based film coating process, various MOFs can be integrated with the cMOF in a layered film structure. This approach enables precise yet independent thickness control over the two MOF layers, offering significant functional tunability to meet the specific requirements of the target applications. Specifically, the thickness of the cMOF layer can be adjusted to enhance the general sensitivity to a wide range of gases, while the thickness of the second MOF layer influences both the sensitivity and selectivity for specific target gases.

Gas Sieving Effect for Enhancing Selectivity. To investigate the effect of the second MOF layer in cMOF-based sensors, we first conducted sensing tests with ZIF-8 on the cMOF films. Pristine cMOFs have been widely employed as NH_3 sensors, demonstrating reasonable sensitivity and reversibility toward NH_3.[36,37] However, cMOF-based NH_3 sensors are susceptible to interference from H_2S, exhibiting a greater response to H_2S than to NH_3, thereby raising a selectivity issue (Figure S11). To address this, we utilized ZIF-8 as a sieving layer to enable the selective detection of NH_3. ZIF-8 is well-known for its gas sieving effect due to its well-defined micropores, which have a pore aperture of 3.4 Å.[38] The H_2S molecule, with a kinetic diameter (3.6 Å) larger than the pore size, can be effectively blocked by the ZIF-8 sieving layer. In contrast, NH_3, with a much smaller kinetic diameter (2.6 Å), can more easily penetrate the ZIF-8 layer. This can result in a reversal of the response to the two gases, making cMOF-based sensors more selective for targeting NH_3. Before the ZIF-8 layer was coated, the NH_3 sensing performance of pristine cMOF films was optimized by controlling the thickness. The cMOF thin films exhibited an approximately 4-fold higher response than drop-coated bulk samples, owing to enhanced gas diffusivity and reactivity in the thin sensing layer (Figure S12). Similarly, thinner films fabricated at faster shearing speeds led to a further increase in response. The thickness of cMOF thin film was then optimized at a shearing speed of 5 mm/s.

On the cMOF thin film, ZIF-8 layers were fabricated at varying shearing speeds, and their NH_3 and H_2S sensing performances were evaluated. Overall, the ZIF-8 overlayer led to a noticeable reduction in NH_3 response and sensing speed (Figures 3a and S13). In particular, a thicker layer fabricated at lower shearing speeds had a more pronounced effect on the NH_3 response. This implies that although the pore diameter is larger than the kinetic diameter of NH_3, the ZIF-8 layer still partially impedes gas diffusion. However, this effect is even more pronounced for larger H_2S molecules, leading to a significant response reduction of up to 92.4% with the ZIF-8 layer (Figures 3b and S14). The strong gas sieving effect of the ZIF-8 layer remained consistent across varying shearing speeds within the evaporation regime. However, a sample fabricated at a shearing speed of 10 mm/s, corresponding to the Landau-

https://doi.org/10.1021/acsnano.4c18848
ACS Nano XXXX, XXX, XXX−XXX

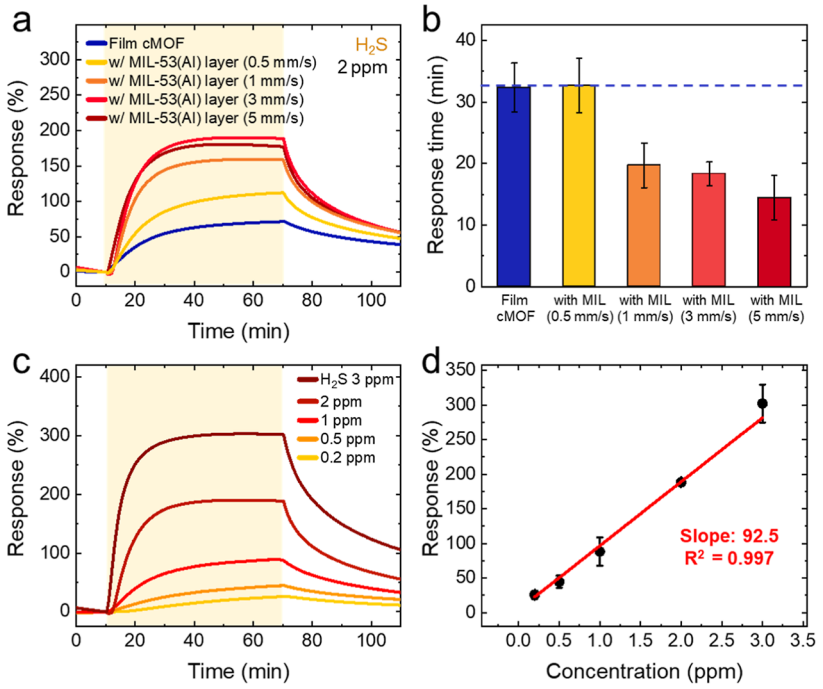

Figure 4. Sensing performance with the MIL-53(Al)-TDC layer. (a) Dynamic sensing traces of the cMOF thin film and MIL-53(Al)-TDC layers fabricated at different shearing speeds toward 2 ppm of H_2S. (b) Response times of MIL-53(Al)-TDC layers fabricated at different shearing speeds. (c) Dynamic sensing traces of the cMOF with a MIL-53(Al)-TDC layer fabricated at a shearing speed of 3 mm/s toward varying concentrations of H_2S and (d) the corresponding response vs concentration graph with linear fitting.

Levich regime, exhibited a significantly weaker sieving effect, likely due to the presence of numerous defects (Figure S10). Based on the relative response of NH_3 and H_2S, the optimal shearing speed for the ZIF-8 layer was determined to be 3 mm/s (Figure 3c). Under the optimized conditions, integrating the ZIF-8 layer with the cMOF resulted in NH_3/H_2S selectivity of 3.62, a significant improvement from the 0.33 observed without ZIF-8, indicating a successful reversal in selectivity.

Figures 3d and S15 display the response traces of ZIF-8 (3 mm/s) on a cMOF sensor to NH_3 at concentrations ranging from 0.2 to 5 ppm. The cMOF sensor exhibited clear and distinct responses across all tested NH_3 concentrations. Although the ZIF-8 layer partially hinders the diffusion of NH_3, the sensitivity of the thin-film sensor is still comparable to other previously reported cMOF sensors (Table S1).[10−12,36,37,39−42] Additionally, the relationship between response and concentration shows good linearity, enabling accurate quantification of the NH_3 concentration within this range (Figure S16). The ZIF-8 layer also suppresses the response to SO_2, which is another interfering gas, potentially due to a larger kinetic diameter (Figure S17). Consequently, the ZIF-8 on the cMOF sensor demonstrates excellent selectivity toward NH_3 over other interfering gases (H_2S, SO_2, ethanol, acetone, and acetylene).

Gas Accumulation Effect for Enhancing Sensitivity. Next, we investigated another function of MOF layers beyond the sieving effect by utilizing the MIL-53(Al)-TDC layer. MIL-53(Al)-TDC features wide pores with a diameter of approximately 9 Å, significantly larger than the kinetic diameter of typical analytes of cMOFs. Therefore, a sieving effect based on the molecular size, as observed in the ZIF-8 layer, is not expected. Instead, MIL-53(Al)-TDC possesses a significantly greater specific surface area (1094.5 m^2/g) than cMOF (259.5 m^2/g), specifically designed for adsorbing H_2S with ultrahigh capacity (18.5 mmol/g) (Figure S18).[31] In addition, the H_2S adsorption is known to be highly reversible, enabling easy desorption and transfer of H_2S to adjacent regions.[31] Based on these properties, we hypothesize that the MIL-53(Al)-TDC layer acts as a H_2S reservoir near the interface with the cMOF, enhancing the effective activity of H_2S and facilitating its reaction with the cMOF to improve H_2S sensitivity.

To test this hypothesis, we fabricated MIL-53(Al)-TDC layers on cMOFs by varying the shearing speed, following a procedure similar to that used for coating the ZIF-8 layer. The cMOF with MIL-53(Al)-TDC layers showed up to a 2.6-fold higher H_2S response compared to that of the pristine cMOF film (Figures 4a and S19). Interestingly, regardless of the thickness of the MIL-53(Al)-TDC layers, no significant reduction in the response speed was observed (Figure 4b). This behavior contrasts with that of the ZIF-8 layer, which considerably reduced the response speed even for smaller NH_3 molecules. Instead, the response speed was accelerated with MIL-53(Al)-TDC layers, as evidenced by decreased response time. This indicates that the role of the MIL-53(Al)-TDC with wide pores is fundamentally different from that of sieving layers such as ZIF-8. It does not significantly hinder H_2S diffusion but, as hypothesized, promotes its surface adsorption and interaction with the cMOF layer. Another notable change by the MIL-53(Al)-TDC layers is the enhancement of the recovery speed. Typically, cMOF-based H_2S sensors operating at room temperature exhibit insufficient recovery owing to the slow desorption of H_2S.[24] While only 45.6% of the H_2S response of the pristine cMOF films is recovered after 40 min in fresh air, the MIL-53(Al)-TDC layers improve the recoverability up to 70.6% (Figure S20). This implies that the MIL-53(Al)-TDC layer not only facilitates the adsorption of H_2S but also enhances its desorption. Meanwhile, the

https://doi.org/10.1021/acsnano.4c18848
ACS Nano XXXX, XXX, XXX−XXX

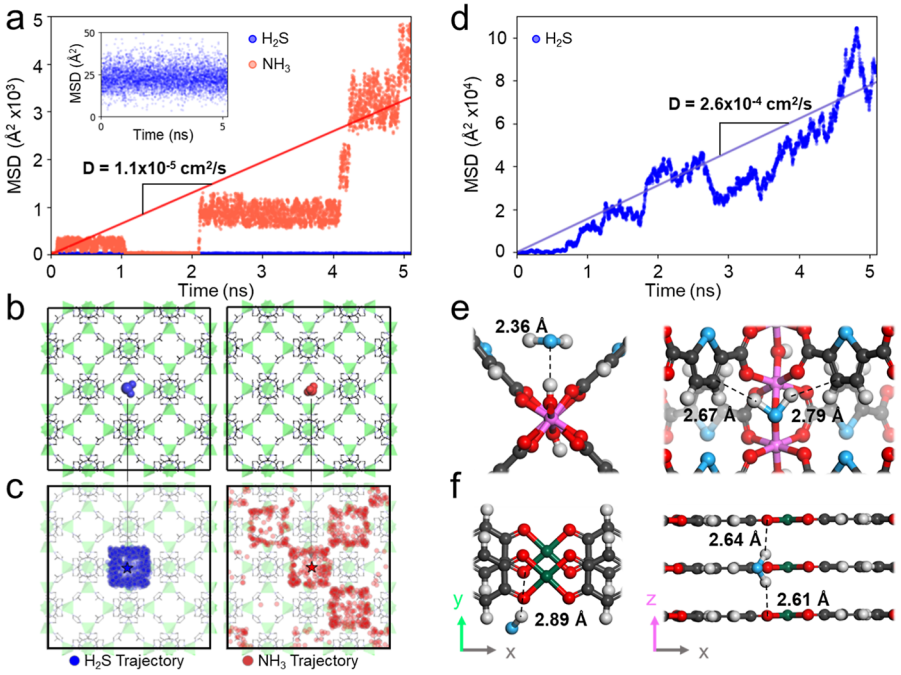

Figure 5. Mechanism study by computational simulation. (a) Calculated MSD of NH_3 and H_2S gas in ZIF-8. The inset figure is an enlarged MSD of H_2S. (b) Initial snapshot of the MD simulation in the ZIF-8 of H_2S and NH_3. Hydrogen atoms in the ZIF-8 are omitted for clarity. (c) Trajectories of H_2S and NH_3 gas during the MD simulation. Star-shaped markers indicate the initial position. (d) Calculated MSD of H_2S gas in the MIL-53(Al)-TDC. DFT optimized binding configuration of H_2S gas in the (e) MIL-53(Al)-TDC and (f) cMOF. Al (purple), Cu (green), S (sky blue), O (red), H (white), and C (black) atoms are represented in the structures.

thickness of the MIL-53(Al)-TDC layer is still a critical factor for H_2S sensing performance, as thinner layers exhibited higher H_2S sensitivity and response speed. This can be attributed to the concentration of the H_2S accumulation layer closer to the interface in thinner MIL-53(Al)-TDC layers, resulting in a greater effect in promoting the reaction with H_2S. Accordingly, the shearing speed was optimized to 3 mm/s, yielding the thinnest layer within the evaporative regime (Figure S8). Under optimized conditions, the MIL-integrated sensors showed good linearity from 0.2 to 3 ppm of H_2S (Figures 4c,d and S21). Specifically, accurate sub-ppm quantification within this range is crucial for disease diagnosis through H_2S sensing as a biomarker in exhaled breath.[43] Overall, the sensing performance is comparable to that of state-of-the-art MOF-based H_2S sensors operating at room temperature, with exceptional recoverability attributed to the MIL-53(Al)-TDC layer (Table S2).[10,12,13,17,20,24,44]

As mentioned above, a large pore diameter is essential to avoid impeding diffusion of the target gas. Additionally, reversible adsorption is a crucial factor as it facilitates the transfer of accumulated gas in the reservoir region to the final sensing layer. MIL-53(Fe) is an isostructural MOF with MIL-53(Al)-TDC, sharing a similar pore diameter. However, its Fe nodes directly bind to and irreversibly react with H_2S, unlike MIL-53(Al)-TDC, thereby suppressing desorption.[45] The MIL-53(Fe) layer on cMOF sensors decreased H_2S sensitivity due to the accumulation of the irreversibly oxidized SO_4^{2-} on the MIL layer (Figure S22).[46] It highlights the importance of reversible adsorption. On the other hand, we employed an MFM-300(Al) layer, which has a wide pore diameter (6.5 Å) and high NO_2 adsorption capacity (14.1 mmol/g) and reversibility.[30,47] In this case, the NO_2 response was enhanced, similar to the effect of the MIL-53(Al)-TDC layer for H_2S (Figure S23). Altogether, we demonstrated that our MOF-on-cMOF fabrication strategy not only facilitates the easy integration of various MOF structures with cMOF but also allows for the rational tuning of sensor selectivity and sensitivity for different target analytes based on the specific characteristics of each MOF (Figure S24).

MD Simulation for Gas Diffusion in the ZIF-8 Layer. MD simulations were conducted to explore the gas-sensing mechanism facilitated by the ZIF-8 layer. H_2S and NH_3 molecules were initially positioned at the center of one of ZIF-8's large pores (Figure S25), and the simulation was performed under room temperature conditions. Notably, H_2S molecules demonstrated negligible diffusion across the ZIF-8 pores, as evidenced by mean square displacement (MSD) values oscillating within the 0−50 $Å^2$ range (Figure 5a). This observation indicates that H_2S molecules remain confined within the initial pore, unable to traverse the ZIF-8 framework (Figure 5b,c and Video S1). As mentioned above, the restricted movement of H_2S is primarily due to the pore aperture of ZIF-8 (3.4 Å) being narrower than the kinetic diameter of H_2S (3.6 Å). Consequently, the incorporation of ZIF-8 layers on cMOF may hinder H_2S diffusion toward the sensing layer and diminish the H_2S response, consistent with the experimental results shown in Figure 3b.

In contrast, NH_3 is expected to exhibit different behavior as its kinetic diameter of 2.6 Å is smaller than the pore size of ZIF-8. Unlike in the case of H_2S, there is a noticeable increase in the MSD of NH_3 over the simulation time, indicating substantial diffusion through the ZIF-8 layers (Figure 5a−c and Video S2). Based on the slope of the MSD over time, the diffusion coefficient (D) for NH_3 was estimated to be 1.1×10^{-5} cm^2/s. This corresponds to a diffusion length of 2790 μm over 60 min of gas exposure for the sensors, which is sufficient to penetrate submicrometer-thick ZIF-8 layers. Therefore, the integration of a ZIF-8 sieving layer onto the cMOF sensor

https://doi.org/10.1021/acsnano.4c18848
ACS Nano XXXX, XXX, XXX−XXX

provides markedly different pore accessibility for H_2S and NH_3, modulating their gas selectivity in a manner consistent with the sensing results.

Computational Analysis of H_2S Sensing in MIL-53(Al)-TDC and cMOF. MIL-53(Al)-TDC features infinite one-dimensional pore channels with a diameter of around 9 Å (Figure S26). This diameter is much larger than the kinetic diameter of H_2S gas, thereby allowing unhindered passage through the MIL-53(Al)-TDC layers. MD simulations revealed a linear increase in the MSD of H_2S gas over time, with the diffusion coefficient calculated to be 2.6×10^{-4} cm^2/s (Figure 5d). This value corresponds to centimeter-scale diffusion length, which exceeds the diffusion rate of the smaller NH_3 molecule in ZIF-8, highlighting pore diameter as a critical parameter. These simulation results align well with the rapid, unhindered response observed in MIL-53(Al)-TDC layered cMOF sensors toward H_2S.

In addition to facile diffusion through the pores, the MIL-53(Al)-TDC layer should enable moderate and reversible adsorption for aiding in the transfer of H_2S gas toward the cMOF sensing layer at the interface. Accordingly, DFT calculations were conducted to further investigate the interactions between H_2S and the MOFs. DFT simulations revealed that MIL-53(Al)-TDC has a moderate binding energy of −0.48 eV for H_2S, occurring when the H atom of the hydroxyl group (μ−OH) bound to the Al(III) center interacted with the S atom of the H_2S molecule (Figure 5e). In cMOF, the optimal binding site for H_2S was identified where the hydrogen atoms of H_2S interact with the oxygen atoms of the HHTP ligand within the pore (Figure 5f). Interestingly, this yields a binding energy of −0.41 eV, similar to that of MIL-53(Al)-TDC. These comparable gas adsorption energies enable the facile transfer of H_2S molecules between the two MOFs, which is advantageous for both the sensing response and recovery performance.

In terms of sensor response, the moderate binding energy of MIL-53(Al)-TDC, combined with its greater surface area and H_2S adsorption capacity, increases the local concentration of H_2S at the interface of the two MOFs. Simultaneously, cMOF, with comparable binding energies, can effectively capture the accumulated H_2S from the MIL-53(Al)-TDC layer. This process facilitates a more rapid and sensitive detection of H_2S gas within the sensing layer. For sensor recovery, MIL-53(Al)-TDC also acts as a secondary binding site for facilitating desorption during the recovery phase.[48,49] This aligns with the improved recoverability observed in the sensing tests. Overall, the computational analysis further substantiates the crucial role of the MOF overlayer for enhancing the sensing performance, specifically through facile diffusion and reversible adsorption.

CONCLUSIONS

In summary, we demonstrate a rational approach to tuning the sensing properties of cMOF-based sensors by integrating them with other MOFs in layered structures. The two-step film fabrication method using solution shearing enables the construction of layered films from various MOFs. The sensing properties of the cMOF sensor were effectively modified based on the pore structure and gas adsorption affinity of the MOFs. Notably, we propose a gas accumulation effect that enhances the sensitivity, response, and recovery speed for different analytes, thereby expanding the conventional role of the MOF layers. Computational analyses reveal that wide pores to facilitate diffusion of target analytes and moderate binding energy to ensure reversibility are critical for achieving the desired sensing performance. This study presents a promising strategy for designing multifunctional sensing platforms by leveraging the versatile properties of conventional MOFs, which can be adapted to complex environments, such as atmospheric conditions and exhaled breath. With the combination of the scalability of the fabrication method, this approach is expected to accelerate the development of MOF-based sensors for real-world applications.

EXPERIMENTAL SECTION

Materials. Copper(II) acetate monohydrate ($Cu(OAc)_2 \cdot H_2O$, 99%), zinc(II) nitrate hexahydrate ($Zn(NO_3)_2 \cdot 6H_2O$, 98%), 2-methylimidazole (2-MIM, 99%), hexadecyltrimethylammonium bromide (CTAB, 98%), dimethyl sulfoxide (DMSO, 99.9%), methanol (99.8%), ethanol (99.5%), aluminum chloride hexahydrate ($AlCl_3 \cdot 6H_2O$, 98%), 2,5-thiophenedicarboxylic acid (99%), dimethylformamide (DMF, 99.8%), iron(III) chloride ($FeCl_3$, 97%), terephthalic acid (98%), aluminum nitrate nonahydrate ($Al(NO_3)_3 \cdot 9H_2O$, 98%), piperazine (99%), and Nitric acid solution (HNO_3, 70%) were purchased from Sigma-Aldrich. 2,3,6,7,10,11-Hexahydroxytriphenylene hydrate (HHTP, 95.0%) and biphenyl-3,3′,5,5′-tetracarboxylic acid (98%) were purchased from Tokyo Chemical Industry.

Synthesis of ZIF-8. Five mL of $Zn(NO_3)_2 \cdot 6H_2O$ solution (0.083 g/mL in methanol) and 5 mL of 2-MIM solution (0.226 g/mL in methanol) were mixed with the addition of 1 mg of CTAB for tuning the size of crystallites.[50] The mixed solution was left to stand for 1.5 h at 30 °C. The resulting white precipitate was washed three times with methanol via centrifugation, followed by drying at 60 °C for 1 h.

Synthesis of MIL-53(Al)-TDC. MIL-53-(Al)-TDC was synthesized according to a previously reported method.[31] First, 65 mg of $AlCl_3$ and 2,5-thiophenedicarboxylic acid were dissolved in 2.5 mL of deionized (DI) water and 1.8 mL of DMF, respectively. The two solutions were mixed in a 25 mL glass vial, and the mixture was stirred for 5 min. The mixture was heated at 100 °C for 5 h and then cooled to room temperature. The remaining reactants in the product were washed three times with DMF through centrifugation. For further washing, the product was reimmersed in DMF at 150 °C for 1 h. To remove DMF molecules from the pores, the product underwent solvent exchange with acetone for 3 days and was dried under vacuum.

Synthesis of MIL-53(Fe). MIL-53(Fe) was synthesized according to a previously reported method.[51] 261.9 mg of $FeCl_3$ and 268.2 mg of terephthalic acid were dissolved in 35 mL of DMF. The solution was transferred to a 50 mL Teflon-lined autoclave and heated at 150 °C for 15 h. The resulting yellow product was filtered and washed with DMF. The product was then reimmersed in DMF and heated at 150 °C for an additional 12 h. To remove DMF, the solid underwent solvent exchange with DI water for 1 day and was then dried under a vacuum.

Synthesis of MFM-300(Al). MFM-300(Al) was prepared following a previously reported method with modifications.[30] 90 mg of biphenyl-3,3′,5,5′-tetracarboxylic acid was dispersed in 7.5 mL of DI water and ultrasonicated for 5 min. Then, 350 mg of $Al(NO_3)_3 \cdot 9H_2O$ and 150 mg of piperazine were dissolved in 7.5 mL of DI water and mixed with the suspension. The mixture was transferred to a 20 mL Teflon lined autoclave, and 3 mL of 3 M aqueous HNO_3 was added, forming a white slurry. The mixture was heated to 210 °C for 3 days. After cooling to room temperature, the resulting white crystalline solid was filtered and washed with DI water and ethanol, followed by drying under vacuum at 80 °C for 12 h.

Fabrication of the Microfluidic Blade. The polyimide (PI) film (Kapton HN film) with 125 μm thickness was ablated in the inlet, outlet, backplate, path, and micro herringbone pattern using a UV laser.[52] To deposit 3 μm FEP nano-powders on the top side of these patterned PI films, we spin-coated them with a fluoroethylene propylene (FEP, ND-110) solution (purchased from DuPont and Daikin). After spin-coating, we evaporated the solvent at 100 °C for 5

https://doi.org/10.1021/acsnano.4c18848
ACS Nano XXXX, XXX, XXX−XXX

min. For alignment and stacking of PI films, four 1 mm diameter holes at the corners were used to fit onto pins on a metal plate. Seven PI films were vertically stacked on that plate. Then, they were baked and pressed at 350 °C under 10 kPa pressure for 5 h in an oven. For the hydrophobic surface treatment, the fabricated microfluidic blade was coated with 5 nm Cr and 50 nm Au by electron-beam evaporation and immersed in 10 mM 1H,1H,2H,2H-perfluorodecanethiol (PFDT) with ethanolic solution for 1 h.

Synthesis of a cMOF Thin Film Using the Microfluidic Solution Shearing Process. $Cu(OAc)_2{\cdot}H_2O$ solution (0.12 mM in DMSO) and HHTP solution (0.10 mM in DMSO) were injected into a microfluidic channel using a syringe pump (PHD ULTRA, Harvard Apparatus) and 2.5 mL syringe (Hamilton 1002 LTN SYR) with a 200 μL/min flow rate. The microfluidic channels were shaped in a herringbone pattern for efficient mixing. The mixed solution was discharged and coated on the UV−ozone-treated (for 20 min) alumina sensor substrate by solution shearing. The substrate temperature, coating speed, tilted angle of the blade, and gap (i.e., the distance between blade and substrate) were 150 °C, 5 mm/s, 30°, and 100 μm, respectively. The synthesized $Cu_3(HHTP)_2$ thin film was washed with DMSO and ethanol.

Fabrication of the MOF Overlayer by the Solution Shearing Process. For preparing the glass blade for solution shearing, a slide glass was sequentially washed with toluene, acetone, and isopropyl alcohol. After the use of an O_2 plasma (80 kW, 1 min), the glass was treated with trichloro-(1H,1H,2H,2H-perfluorooctyl)-silane (FTS) by chemical vapor deposition at 70 °C for 30 min. The various MOFs (ZIF-8, MIL-53(Al)-TDC, MIL-53(Fe), and MFM-300(Al)) were thoroughly ground and dispersed in ethanol at a concentration of 100 mg/mL with sonication for 20 min. The MOF suspension was then directly coated on the surface of the $Cu_3(HHTP)_2$ thin film by solution shearing with a glass blade. The substrate temperature, tilted angle of the blade, and gap (i.e., distance between blade and substrate) were 65, 8 °C, and 100 μm, respectively. The coating speed was adjusted to control the thickness of the MOF layers.

Computational Details on DFT Simulation. In our computational study, the structures of MIL-53(Al)-TDC and $Cu_3(HHTP)_2$ were manually constructed using the unit cell and atomic coordinates reported by Tschense et al.[53] and Jeon et al.,[54] respectively. The ZIF-8 structure with a cubic lattice and an I-43 M symmetry group was taken from Fairen-Jimenez et al.[55] Initial optimization of these structures was performed using the Vienna Ab initio Simulation Package (VASP) v.5.4.1 software.[56] The exchange−correlation interaction was treated using the generalized gradient approximation and the projector augmented-wave method. The Perdew−Burke−Ernzerhof functional and Grimme's D3 dispersion were employed to enhance the accuracy of intermolecular interactions.[57,58] A cutoff energy of 520 eV for the plane wave basis set was established. The convergence criteria for electronic and ionic optimization were rigorously set to 1×10^{-5} eV and 0.003 eV/Å, respectively. For the determination of DFT binding energies between the MOFs and gas molecules, the formula $E_{binding} = E_{MOF+Gas} - E_{MOF} - E_{Gas}$ was used. Furthermore, various gas adsorption configurations and the influence of stacking modes in 2D MOFs were considered to investigate the optimal binding sites.[54,59] The computational setup included gamma-centered k-point grids of $2 \times 4 \times 2$ and $1 \times 1 \times 1$ for the calculations concerning MIL-53(Al)-TDC and ZIF-8, respectively. Additionally, for the analysis of the stacked and slab structures of $Cu_3(HHTP)_2$, k-point grids of $1 \times 1 \times 3$ and $1 \times 1 \times 1$ were, respectively, utilized.

MD Simulation. The MD simulations were executed to investigate gas diffusion within MOFs using the large-scale atomic/molecular massively parallel simulator software.[60] For these simulations, the *NVT* ensemble (constant number of particles, volume, and temperature) was employed. The force field parameters for H_2S[61] and NH_3[62] gases were sourced from the transferable potentials for the phase equilibria database. The gas molecules were treated as rigid entities, while the MOFs were allowed flexibility by implementing intramolecular force field parameters.[63] To accurately model molecular interactions within the system, both Lennard-Jones and Coulombic potentials were utilized. The charge values for the MOFs were determined using the PACMOF python library, a machine learning tool trained on a database of DFT-derived charges.[64] The simulation was conducted over a duration of 5 ns with a time step of 1 fs at conditions of 298 K and 1 bar pressure. To assess the mobility of gas molecules within the MOF structure, the MSD was calculated at intervals of 1000 fs. Analysis of the MSD versus time plot allowed for the extraction of the diffusion coefficient (D) by fitting the linear region according to the Einstein relation (D = Slope/6).

Characterizations. SEM and energy-dispersive X-ray spectroscopy (EDS) analyses of MOF thin films were conducted with a Magellan 400 (FEI company). Film thicknesses of samples were measured by a P-15 Long Scan Profiler (KLA). The chemical states of samples were investigated through X-ray photoelectron spectroscopy (XPS) using a Nexsa G2 (Thermo Scientific). Binding energy calibration of the XPS spectra was conducted using an adventitious carbon peak at 284.8 eV. XRD analysis was conducted with a SmartLab (Rigaku) utilizing a Cu $K_{\alpha 1}$ incidence beam. N_2 isotherm analysis was carried out using a 3Flex instrument (Micrometrics). The surface areas of the samples were determined through the Brunauer−Emmett−Teller (BET) method.

Gas-Sensing Measurement. As sensor substrates, alumina plates (2.5 × 2.5 × 0.2 mm) were patterned with interdigitated gold electrodes with a 75 μm gap between them. To fabricate sensors from bulk powder, 5 μL of an ethanol suspension containing sensing materials (10 mg/mL) was drop-coated onto the sensor substrate three times. Sensing tests were conducted in a sealed chamber with controlled injection of gas flow by a mass flow controller. Before injecting the target gas, the sensors were stabilized under dry air for at least 3 h. Real-time changes in sensor resistances were measured by using data acquisition equipment (Keysight 34972). The response of the sensors was calculated using the formula $[(\Delta R/R_0) \times 100]$, where R_0 represents the baseline resistance after stabilization under air, and ΔR represents the change in resistance upon exposure to the target gas. Response time is defined as the time required to reach 90% of the maximum resistance change during gas exposure. Error bars of the response were derived from more than three independent sensors.

ASSOCIATED CONTENT

Supporting Information

The Supporting Information is available free of charge at https://pubs.acs.org/doi/10.1021/acsnano.4c18848.

Additional characterization data for the samples, including SEM, XRD, N_2 isotherm, and XPS analyses, details of the thin-film fabrication process, dynamic sensing data of individual sensors, sensing properties with other MOF layers, including MFM-300(Al) and MIL-53(Fe), and comparison of the sensing performances of cMOF-based sensors reported in the literature (PDF)

MD simulations for diffusion of H_2S in the ZIF-8 layer (MP4)

MD simulations for diffusion of NH_3 in the ZIF-8 layer (MP4)

AUTHOR INFORMATION

Corresponding Authors

Jihan Kim − *Department of Chemical and Biomolecular Engineering, Korea Advanced Institute of Science and Technology (KAIST), Daejeon 34141, Republic of Korea;* orcid.org/0000-0002-3844-8789; Email: jihankim@kaist.ac.kr

Steve Park − *Department of Materials Science and Engineering, Korea Advanced Institute of Science and Technology (KAIST), Daejeon 34141, Republic of Korea;* Email: stevepark@kaist.ac.kr

https://doi.org/10.1021/acsnano.4c18848
ACS Nano XXXX, XXX, XXX−XXX

Il-Doo Kim − *Department of Materials Science and Engineering, Korea Advanced Institute of Science and Technology (KAIST), Daejeon 34141, Republic of Korea;* orcid.org/0000-0002-9970-2218; Email: idkim@kaist.ac.kr

Authors

Chungseong Park − *Department of Materials Science and Engineering, Korea Advanced Institute of Science and Technology (KAIST), Daejeon 34141, Republic of Korea*

Junhee Woo − *Department of Materials Science and Engineering, Korea Advanced Institute of Science and Technology (KAIST), Daejeon 34141, Republic of Korea*

Mingyu Jeon − *Department of Chemical and Biomolecular Engineering, Korea Advanced Institute of Science and Technology (KAIST), Daejeon 34141, Republic of Korea;* orcid.org/0000-0002-8285-5197

Jong Won Baek − *Department of Materials Science and Engineering, Korea Advanced Institute of Science and Technology (KAIST), Daejeon 34141, Republic of Korea*

Euichul Shin − *Department of Materials Science and Engineering, Korea Advanced Institute of Science and Technology (KAIST), Daejeon 34141, Republic of Korea*

Complete contact information is available at: https://pubs.acs.org/10.1021/acsnano.4c18848

Author Contributions

§C.P., J.W., and M.J. contributed equally to this work.

Notes

The authors declare no competing financial interest.

ACKNOWLEDGMENTS

All authors contributed to the writing of the manuscript. All authors discussed the results and the manuscript. This research was supported by the Nano & Material Technology Development Program through the National Research Foundation of Korea (NRF) funded by the Ministry of Science and ICT (MSIT) (no. RS-2024-00412249). This work was also supported by the NRF grant funded by the MSIT (no. RS-2024-00435493).

REFERENCES

(1) Li, H.-Y.; Zhao, S.-N.; Zang, S.-Q.; Li, J. Functional metal−organic frameworks as effective sensors of gases and volatile compounds. *Chem. Soc. Rev.* **2020**, *49* (17), 6364−6401.

(2) Islamoglu, T.; Chen, Z.; Wasson, M. C.; Buru, C. T.; Kirlikovali, K. O.; Afrin, U.; Mian, M. R.; Farha, O. K. Metal−organic frameworks against toxic chemicals. *Chem. Rev.* **2020**, *120* (16), 8130−8160.

(3) Shen, Y.; Tissot, A.; Serre, C. Recent progress on MOF-based optical sensors for VOC sensing. *Chem. Sci.* **2022**, *13* (47), 13978−14007.

(4) Zhai, Z.; Zhang, X.; Hao, X.; Niu, B.; Li, C. Metal−organic frameworks materials for capacitive gas sensors. *Adv. Mater. Technol.* **2021**, *6* (10), 2100127.

(5) Lv, Y.; Xu, P.; Yu, H.; Xu, J.; Li, X. Ni-MOF-74 as sensing material for resonant-gravimetric detection of ppb-level CO. *Sens. Actuators, B* **2018**, *262*, 562−569.

(6) Koo, W.-T.; Jang, J.-S.; Kim, I.-D. Metal-Organic Frameworks for Chemiresistive Sensors. *Chem* **2019**, *5* (8), 1938−1963.

(7) Wang, M.; Dong, R.; Feng, X. Two-dimensional conjugated metal−organic frameworks (2D c-MOFs): chemistry and function for MOFtronics. *Chem. Soc. Rev.* **2021**, *50* (4), 2764−2793.

(8) Park, C.; Baek, J. W.; Shin, E.; Kim, I.-D. Two-Dimensional Electrically Conductive Metal−Organic Frameworks as Chemiresistive Sensors. *ACS Nanosci. Au.* **2023**, *3* (5), 353−374.

(9) Jo, Y. M.; Jo, Y. K.; Lee, J. H.; Jang, H. W.; Hwang, I. S.; Yoo, D. J. MOF-based chemiresistive gas sensors: toward new functionalities. *Adv. Mater.* **2023**, *35* (43), 2206842.

(10) Smith, M. K.; Jensen, K. E.; Pivak, P. A.; Mirica, K. A. Direct self-assembly of conductive nanorods of metal−organic frameworks into chemiresistive devices on shrinkable polymer films. *Chem. Mater.* **2016**, *28* (15), 5264−5268.

(11) Campbell, M. G.; Sheberla, D.; Liu, S. F.; Swager, T. M.; Dincă, M. Cu_3(hexaiminotriphenylene)$_2$: An Electrically Conductive 2D Metal−Organic Framework for Chemiresistive Sensing. *Angew. Chem., Int. Ed.* **2015**, *54* (14), 4349−4352.

(12) Meng, Z.; Aykanat, A.; Mirica, K. A. Welding metallophthalocyanines into bimetallic molecular meshes for ultrasensitive, low-power chemiresistive detection of gases. *J. Am. Chem. Soc.* **2019**, *141* (5), 2046−2053.

(13) Jeon, M.; Lee, J.-S.; Kim, M.; Seo, J.-W.; Kim, H.; Moon, H. R.; Choi, S.-J.; Kim, J. Triphenylene-Based 2D cMOFs: Unraveling the H_2S Sensing Mechanism and Applications for a Real-Time Wireless Chemiresistive Sensor. *ACS Appl. Mater. Interfaces* **2024**, *16* (45), 62382−62391.

(14) Park, C.; Shin, H.; Jeon, M.; Cho, S.-H.; Kim, J.; Kim, I.-D. Single-Atom Catalysts in Conductive Metal−Organic Frameworks: Enabling Reversible Gas Sensing at Room Temperature. *ACS Nano* **2024**, *18* (38), 26066−26075.

(15) Koo, W.-T.; Kim, S.-J.; Jang, J.-S.; Kim, D.-H.; Kim, I.-D. Catalytic Metal Nanoparticles Embedded in Conductive Metal−Organic Frameworks for Chemiresistors: Highly Active and Conductive Porous Materials. *Adv. Sci.* **2019**, *6* (21), 1900250.

(16) Park, C.; Koo, W.-T.; Chong, S.; Shin, H.; Kim, Y. H.; Cho, H.-J.; Jang, J.-S.; Kim, D.-H.; Lee, J.; Park, S.; et al. Confinement of Ultrasmall Bimetallic Nanoparticles in Conductive Metal−Organic Frameworks via Site-Specific Nucleation. *Adv. Mater.* **2021**, *33* (38), 2101216.

(17) Sun, Y.; Wang, B.; Hou, Y.; Suematsu, K.; Zhao, Z.; Zhang, W.; Shimanoe, K.; Hu, J. Noble metal nanoparticles functionalized conductive Co_3(hexaiminotriphenylene)$_2$ chemiresistor for hydrogen sulfide detection at Room-Temperature. *Chem. Eng. J.* **2023**, *465*, 142818.

(18) Jo, Y.-M.; Lim, K.; Yoon, J. W.; Jo, Y. K.; Moon, Y. K.; Jang, H. W.; Lee, J.-H. Visible-Light-Activated Type II Heterojunction in Cu_3(hexahydroxytriphenylene)$_2$/Fe_2O_3 Hybrids for Reversible NO_2 Sensing: Critical Role of $\pi-\pi^*$ Transition. *ACS Cent. Sci.* **2021**, *7* (7), 1176−1182.

(19) Roh, H.; Kim, D. H.; Cho, Y.; Jo, Y. M.; Del Alamo, J. A.; Kulik, H. J.; Dincă, M.; Gumyusenge, A. Robust Chemiresistive Behavior in Conductive Polymer/MOF Composites. *Adv. Mater.* **2024**, *36* (27), 2312382.

(20) Cho, S.; Park, C.; Jeon, M.; Hwa Lee, J.; Kwon, O.; Seong, S.; Kim, J.; Kim, I.-D.; Ri Moon, H. Interface-Sensitized Chemiresistor: Integrated Conductive and Porous Metal-Organic Frameworks. *Chem. Eng. J.* **2022**, *449*, 137780.

(21) Kwon, O.; Kim, J. Y.; Park, S.; Lee, J. H.; Ha, J.; Park, H.; Moon, H. R.; Kim, J. Computer-aided discovery of connected metal-organic frameworks. *Nat. Commun.* **2019**, *10* (1), 3620.

(22) Yao, M.-S.; Xiu, J.-W.; Huang, Q.-Q.; Li, W.-H.; Wu, W.-W.; Wu, A.-Q.; Cao, L.-A.; Deng, W.-H.; Wang, G.-E.; Xu, G. Van der Waals Heterostructured MOF-on-MOF Thin Films: Cascading Functionality to Realize Advanced Chemiresistive Sensing. *Angew. Chem., Int. Ed.* **2019**, *58* (42), 14915−14919.

(23) Kim, J.-O.; Koo, W.-T.; Kim, H.; Park, C.; Lee, T.; Hutomo, C. A.; Choi, S. Q.; Kim, D. S.; Kim, I.-D.; Park, S. Large-area synthesis of nanoscopic catalyst-decorated conductive MOF film using microfluidic-based solution shearing. *Nat. Commun.* **2021**, *12* (1), 4294.

(24) Lee, T.; Kim, J.-O.; Park, C.; Kim, H.; Kim, M.; Park, H.; Kim, I.; Ko, J.; Pak, K.; Choi, S. Q.; et al. Large-Area Synthesis of Ultrathin, Flexible, and Transparent Conductive Metal−Organic Framework

Thin Films via a Microfluidic-Based Solution Shearing Process. *Adv. Mater.* **2022**, *34* (12), 2107696.
(25) Hmadeh, M.; Lu, Z.; Liu, Z.; Gándara, F.; Furukawa, H.; Wan, S.; Augustyn, V.; Chang, R.; Liao, L.; Zhou, F.; et al. New porous crystals of extended metal-catecholates. *Chem. Mater.* **2012**, *24* (18), 3511−3513.
(26) Lee, J. C.; Woo, J. H.; Lee, H. J.; Lee, M.; Woo, H.; Baek, S.; Nam, J.; Sim, J. y.; Park, S. Microfluidic Screening-Assisted Machine Learning to Investigate Vertical Phase Separation of Small Molecule: Polymer Blend. *Adv. Mater.* **2022**, *34* (7), 2107596.
(27) Lee, J. C.; Lee, M.; Lee, H. J.; Ahn, K.; Nam, J.; Park, S. Numerical Simulations and In Situ Optical Microscopy Connecting Flow Pattern, Crystallization, and Thin-Film Properties for Organic Transistors with Superior Device-to-Device Uniformity. *Adv. Mater.* **2020**, *32* (48), 2004864.
(28) Cho, J.; Oh, J.; Bang, J.; Koh, J. H.; Jeong, H. Y.; Chung, S.; Son, J. G. Roll-to-plate 0.1-second shear-rolling process at elevated temperature for highly aligned nanopatterns. *Nat. Commun.* **2023**, *14* (1), 8412.
(29) Bux, H.; Liang, F.; Li, Y.; Cravillon, J.; Wiebcke, M.; Caro, J. r. Zeolitic imidazolate framework membrane with molecular sieving properties by microwave-assisted solvothermal synthesis. *J. Am. Chem. Soc.* **2009**, *131* (44), 16000−16001.
(30) Han, X.; Godfrey, H. G.; Briggs, L.; Davies, A. J.; Cheng, Y.; Daemen, L. L.; Sheveleva, A. M.; Tuna, F.; McInnes, E. J.; Sun, J.; et al. Reversible adsorption of nitrogen dioxide within a robust porous metal−organic framework. *Nat. Mater.* **2018**, *17* (8), 691−696.
(31) Zárate, J. A.; Sánchez-González, E.; Jurado-Vázquez, T.; Gutiérrez-Alejandre, A.; González-Zamora, E.; Castillo, I.; Maurin, G.; Ibarra, I. A. Outstanding reversible H_2S capture by an Al (iii)-based MOF. *Chem. Commun.* **2019**, *55* (21), 3049−3052.
(32) Gu, X.; Shaw, L.; Gu, K.; Toney, M. F.; Bao, Z. The meniscus-guided deposition of semiconducting polymers. *Nat. Commun.* **2018**, *9* (1), 534.
(33) Giri, G.; Verploegen, E.; Mannsfeld, S. C.; Atahan-Evrenk, S.; Kim, D. H.; Lee, S. Y.; Becerril, H. A.; Aspuru-Guzik, A.; Toney, M. F.; Bao, Z. Tuning charge transport in solution-sheared organic semiconductors using lattice strain. *Nature* **2011**, *480* (7378), 504−508.
(34) Faustini, M.; Louis, B.; Albouy, P. A.; Kuemmel, M.; Grosso, D. Preparation of sol− gel films by dip-coating in extreme conditions. *J. Phys. Chem. C* **2010**, *114* (17), 7637−7645.
(35) Le Berre, M.; Chen, Y.; Baigl, D. From convective assembly to Landau− Levich deposition of multilayered phospholipid films of controlled thickness. *Langmuir* **2009**, *25* (5), 2554−2557.
(36) Yao, M.-S.; Wang, P.; Gu, Y.-F.; Koganezawa, T.; Ashitani, H.; Kubota, Y.; Wang, Z.-M.; Fan, Z.-Y.; Otake, K.-i.; Kitagawa, S. A comparative study of honeycomb-like 2D π-conjugated metal−organic framework chemiresistors: conductivity and channels. *Dalton Trans.* **2021**, *50* (38), 13236−13245.
(37) Yao, M.-S.; Lv, X.-J.; Fu, Z.-H.; Li, W.-H.; Deng, W.-H.; Wu, G.-D.; Xu, G. Layer-by-Layer Assembled Conductive Metal−Organic Framework Nanofilms for Room-Temperature Chemiresistive Sensing. *Angew. Chem., Int. Ed.* **2017**, *56* (52), 16510−16514.
(38) Kim, D.-H.; Chong, S.; Park, C.; Ahn, J.; Jang, J.-S.; Kim, J.; Kim, I.-D. Oxide/ZIF-8 Hybrid Nanofiber Yarns: Heightened Surface Activity for Exceptional Chemiresistive Sensing. *Adv. Mater.* **2022**, *34* (10), 2105869.
(39) Wu, A.-Q.; Wang, W.-Q.; Zhan, H.-B.; Cao, L.-A.; Ye, X.-L.; Zheng, J.-J.; Kumar, P. N.; Chiranjeevulu, K.; Deng, W.-H.; Wang, G.-E.; et al. Layer-by-layer assembled dual-ligand conductive MOF nanofilms with modulated chemiresistive sensitivity and selectivity. *Nano Res.* **2021**, *14* (2), 438−443.
(40) Chen, X.; Lu, Y.; Dong, J.; Ma, L.; Yi, Z.; Wang, Y.; Wang, L.; Wang, S.; Zhao, Y.; Huang, J.; et al. Ultrafast In Situ Synthesis of Large-Area Conductive Metal−Organic Frameworks on Substrates for Flexible Chemiresistive Sensing. *ACS Appl. Mater. Interfaces* **2020**, *12* (51), 57235−57244.
(41) Zheng, R.; Fu, Z. H.; Deng, W. H.; Wen, Y.; Wu, A. Q.; Ye, X. L.; Xu, G. The growth mechanism of a conductive MOF thin film in spray-based layer-by-layer liquid phase epitaxy. *Angew. Chem., Int. Ed.* **2022**, *61* (43), No. e202212797.
(42) Lin, Y.; Li, W. H.; Wen, Y.; Wang, G. E.; Ye, X. L.; Xu, G. Layer-by-layer growth of preferred-oriented MOF thin film on nanowire array for high-performance chemiresistive sensing. *Angew. Chem., Int. Ed.* **2021**, *60* (49), 25758−25761.
(43) Tangerman, A.; Winkel, E. Extra-oral halitosis: an overview. *J. Breath Res.* **2010**, *4* (1), 017003.
(44) Smith, M. K.; Mirica, K. A. Self-Organized Frameworks on Textiles (SOFT): Conductive Fabrics for Simultaneous Sensing, Capture, and Filtration of Gases. *J. Am. Chem. Soc.* **2017**, *139* (46), 16759−16767.
(45) Hamon, L.; Serre, C.; Devic, T.; Loiseau, T.; Millange, F.; Férey, G.; Weireld, G. D. Comparative study of hydrogen sulfide adsorption in the MIL-53 (Al, Cr, Fe), MIL-47 (V), MIL-100 (Cr), and MIL-101 (Cr) metal− organic frameworks at room temperature. *J. Am. Chem. Soc.* **2009**, *131* (25), 8775−8777.
(46) Zheng, X.-X.; Fang, Z.-P.; Dai, Z.-J.; Cai, J.-M.; Shen, L.-J.; Zhang, Y.-F.; Au, C.-T.; Jiang, L.-L. Iron-based metal−organic frameworks as platform for H2S selective conversion: structure-dependent desulfurization activity. *Inorg. Chem.* **2020**, *59* (7), 4483−4492.
(47) Han, Y.; Chen, Y.; Ma, Y.; Bailey, J.; Wang, Z.; Lee, D.; Sheveleva, A. M.; Tuna, F.; McInnes, E. J.; Frogley, M. D.; et al. Control of the pore chemistry in metal-organic frameworks for efficient adsorption of benzene and separation of benzene/cyclohexane. *Chem* **2023**, *9* (3), 739−754.
(48) Cho, S. R.; Kim, D. H.; Jeon, M.; Rani, P.; Gyeon, M.; Kim, Y.; Jo, M. k.; Song, S.; Park, J. Y.; Kim, J.; et al. Overlaying monolayer metal−organic framework on $PtSe_2$-based gas sensor for tuning selectivity. *Adv. Funct. Mater.* **2022**, *32* (47), 2207265.
(49) Jang, J. S.; Jung, H. J.; Chong, S.; Kim, D. H.; Kim, J.; Kim, S. O.; Kim, I. D. 2D materials decorated with ultrathin and porous graphene oxide for high stability and selective surface activity. *Adv. Mater.* **2020**, *32* (36), 2002723.
(50) Pan, Y.; Heryadi, D.; Zhou, F.; Zhao, L.; Lestari, G.; Su, H.; Lai, Z. Tuning the crystal morphology and size of zeolitic imidazolate framework-8 in aqueous solution by surfactants. *CrystEngComm* **2011**, *13* (23), 6937−6940.
(51) Horcajada, P.; Serre, C.; Maurin, G.; Ramsahye, N. A.; Balas, F.; Vallet-Regí, M.; Sebban, M.; Taulelle, F.; Férey, G. Flexible porous metal-organic frameworks for a controlled drug delivery. *J. Am. Chem. Soc.* **2008**, *130* (21), 6774−6780.
(52) Kim, H.; Min, K.-I.; Inoue, K.; Im, D. J.; Kim, D.-P.; Yoshida, J.-i. Submillisecond organic synthesis: Outpacing Fries rearrangement through microfluidic rapid mixing. *Science* **2016**, *352* (6286), 691−694.
(53) Tschense, C. B.; Reimer, N.; Hsu, C. W.; Reinsch, H.; Siegel, R.; Chen, W. J.; Lin, C. H.; Cadiau, A.; Serre, C.; Senker, J.; et al. New Group 13 MIL-53 Derivates based on 2, 5-Thiophenedicarboxylic Acid. *Z. Anorg. Allg. Chem.* **2017**, *643* (21), 1600−1608.
(54) Jeon, M.; Kim, M.; Lee, J.-S.; Kim, H.; Choi, S.-J.; Moon, H. R.; Kim, J. Computational Prediction of Stacking Mode in Conductive Two-Dimensional Metal−Organic Frameworks: An Exploration of Chemical and Electrical Property Changes. *ACS Sens.* **2023**, *8* (8), 3068−3075.
(55) Fairen-Jimenez, D.; Moggach, S.; Wharmby, M. T.; Wright, P. A.; Parsons, S.; Duren, T. Opening the gate: framework flexibility in ZIF-8 explored by experiments and simulations. *J. Am. Chem. Soc.* **2011**, *133* (23), 8900−8902.
(56) Kresse, G.; Furthmüller, J. Efficient iterative schemes for ab initio total-energy calculations using a plane-wave basis set. *Phys. Rev. B* **1996**, *54* (16), 11169.
(57) Perdew, J. P.; Burke, K.; Ernzerhof, M. Generalized Gradient Approximation Made Simple. *Phys. Rev. Lett.* **1996**, *77* (18), 3865−3868.

https://doi.org/10.1021/acsnano.4c18848
ACS Nano XXXX, XXX, XXX−XXX

(58) Grimme, S.; Antony, J.; Ehrlich, S.; Krieg, H. A consistent and accurate ab initio parametrization of density functional dispersion correction (DFT-D) for the 94 elements H-Pu. *J. Chem. Phys.* **2010**, *132* (15), 154104.
(59) Zhang, Z.; Valente, D. S.; Shi, Y.; Limbu, D. K.; Momeni, M. R.; Shakib, F. A. In silico high-throughput design and prediction of structural and electronic properties of low-dimensional metal−organic frameworks. *ACS Appl. Mater. Interfaces* **2023**, *15* (7), 9494−9507.
(60) Plimpton, S. Fast parallel algorithms for short-range molecular dynamics. *J. Comput. Phys.* **1995**, *117* (1), 1−19.
(61) Shah, M. S.; Tsapatsis, M.; Siepmann, J. I. Development of the transferable potentials for phase equilibria model for hydrogen sulfide. *J. Phys. Chem. B* **2015**, *119* (23), 7041−7052.
(62) Zhang, L.; Siepmann, J. I. Development of the TraPPE force field for ammonia. *Collect. Czech. Chem. Commun.* **2010**, *75* (5), 577−591.
(63) Boyd, P. G.; Moosavi, S. M.; Witman, M.; Smit, B. Force-field prediction of materials properties in metal-organic frameworks. *J. Phys. Chem. Lett.* **2017**, *8* (2), 357−363.
(64) Kancharlapalli, S.; Gopalan, A.; Haranczyk, M.; Snurr, R. Q. Fast and accurate machine learning strategy for calculating partial atomic charges in metal−organic frameworks. *J. Chem. Theory Comput.* **2021**, *17* (5), 3052−3064.

https://doi.org/10.1021/acsnano.4c18848
ACS Nano XXXX, XXX, XXX−XXX